Chemical Science

ROYAL SOCIETY OF CHEMISTRY

EDGE ARTICLE

View Article Online
View Journal



Cite this: DOI: 10.1039/d6sc02569b

All publication charges for this article have been paid for by the Royal Society of Chemistry

# Pendant amine-promoted complete eight-electron photoreduction of $CO_2$ to methane by a molecular nickel catalyst

Chandan Das,[a] Liton Seikh,[a] Abhishek Saini,[a] Gazal Sabharwal,[a] Somnath Guria,[a] Piyali Majumder,[a] Maravanji S. Balakrishna,[a] Goutam K. Lahiri[a] and Arnab Dutta *[abc]

Received 28th March 2026
Accepted 3rd June 2026

DOI: 10.1039/d6sc02569b

rsc.li/chemical-science

Solar-driven $CO_2$ reduction offers a sustainable route to carbon neutrality by converting greenhouse gases into value-added fuels. Here, we report a secondary coordination sphere design strategy that directs $CO_2$ photoreduction selectivity toward methane ($CH_4$). A redox-active Ni complex (**C1**), incorporating two (6-amino-2-(phenylazo)pyridine) ligands with a pendant amine, exhibits markedly enhanced $CH_4$ selectivity compared to control complexes lacking the pendant $-NH_2$ group. Systematic evaluation of sacrificial donors, proton sources, and photosensitizers identified a dimeric Cu(I)-based photosensitizer (**Cu-PS-1**) as a cost-effective alternative to Ir-based systems, achieving $TON_{CO_2\rightarrow CO} = 4789$, $TON_{CO_2\rightarrow CH_4} = 1130$, and $TON_{CO\rightarrow CH_4} = 3102$, rivalling **Ir-PS-1**. *Operando* UV-vis, FTIR, and EPR spectroscopy, together with DFT calculations, revealed a stepwise $8e^-/8H^+$ reduction pathway in which the pendant $-NH_2$ group stabilizes key COOH and $CH_x$ intermediates through hydrogen bonding, lowering activation barriers and steering selectivity toward $CH_4$. These results establish OCS engineering as a powerful design principle for earth-abundant molecular catalysts and highlight new opportunities for selective $CO_2$-to-$CH_4$ conversion in artificial photosynthesis and carbon valorization.

## Introduction

The growing demand for circularity and sustainable resources has highlighted the possibility of using carbon dioxide ($CO_2$) as a feedstock to produce fuels and fine chemicals. Given these developments, solar-driven $CO_2$ reduction offers a sustainable way to convert solar energy while simultaneously addressing global warming concerns.[1–5] Converting solar energy into chemical energy is particularly appealing, as it enables long-term and reliable energy storage compatible with existing infrastructure. However, the $CO_2$ reduction step remains inherently slow due to the high thermodynamic stability of the molecule. Furthermore, achieving selectivity in the $CO_2$ reduction process is challenging due to the possibility of generating numerous carbonaceous products in variable oxidation states,[4] compounded by the rapid kinetics of the competing hydrogen evolution reaction (HER) under reductive conditions. To overcome these challenges, there is a growing need for efficient and selective catalysts that are both rationally designed and economically viable. Recent years have witnessed growing interest in molecular catalysts that employ cost-effective first-row transition metals.[6–8] Among them, earth-abundant nickel has emerged as an attractive alternative to leading 4d and 5d-metal-based catalysts (such as palladium and platinum).[9,10] Nickel can readily access multiple oxidation states, a property that underpins its catalytic versatility. Its central role in [NiFe] CO-dehydrogenases (CODHs), which facilitate the reversible conversion of $CO_2$ to CO, makes it a highly attractive candidate for photocatalytic $CO_2$ reduction.[11,12] Consequently, nickel complexes have been extensively explored as molecular catalysts for $CO_2$ reduction. A series of mononuclear Ni-based catalysts, including Ni–$N_2S_2$ complexes,[13,14] N-heterocyclic carbene (NHC) complexes,[15,16] Ni-macrocyclic complexes,[17–21] nickel polypyridine[22,23] and other Ni-based[24–26] complexes, have demonstrated the capability to convert $CO_2$ to CO *via* a $2e^-/2H^+$ pathway. These studies highlight how both photochemical and electrochemical approaches can be employed to achieve efficient $CO_2$ conversion using earth-abundant metal catalysts, sometimes even in the absence of metal-based photosensitizers. Despite these improvements, the production of fully reduced **C1** species $CH_4$ from $CO_2$ and CO through the $8e^-/8H^+$ or $6e^-/6H^+$ pathways, respectively, remains a significant challenge. To date, only a limited number of studies have reported the production of $CH_4$ from $CO_2$ and CO using 3d metal-based catalysts *via* photochemical pathways. Robert and co-workers[27] pioneered

[a]*Department of Chemistry, Indian Institute of Technology Bombay, Powai, Mumbai 400076, India. E-mail: arnab.dutta@iitb.ac.in*

[b]*Centre for Climate Studies, Indian Institute of Technology Bombay, Powai, Mumbai 400076, India*

[c]*National Centre of Excellence CCUS, Indian Institute of Technology Bombay, Powai, Mumbai 400076, India*

this field by employing an Fe-based molecular catalyst for the photocatalytic production of $CH_4$ from $CO_2$ and CO in the presence of triethanolamine (TEOA) as an electron donor under 420 nm light irradiation, achieving turnover numbers (TON) of 367 for CO and 159 for $CH_4$, respectively (Fig. 1). Later, the same group[28] extended this work by modifying the photocatalytic conditions, using 5,10-di(2-naphthyl)-5,10-dihydrophenazine and 3,7-di(4-biphenyl)-1-naphthalene 10-phenoxazine as organic photosensitizers and TEOA as an electron donor under 435 nm light irradiation (Fig. 1). Recently, Delcamp and co-workers[16] have strategically designed a novel series of Ni-based catalysts featuring a redox-active macrocyclic ligand bearing a bipyridyl N-heterocyclic carbene. These catalysts achieved the conversion of $CO_2$ to $CH_4$ with a TON of up to 19 000 in the presence of $Ir(ppy)_3$ as a photosensitizer (PS) and BIH as an electron donor under simulated solar light irradiation (Fig. 1). Ir-based photosensitizers (Ir-PS) are widely utilized due to their high photo-stability, strong visible-light absorption, extended excited-state lifetime, and strong reducing strength in the excited state.[29,30] Yet, the prohibitive cost and synthetic complexity of Ir-based photosensitizers remain major barriers to their practical use in $CO_2$-to-$CH_4$ conversion. Hence, there is a growing demand for cost-effective and sustainable alternatives. Researchers are actively exploring replacements such as organic (π-conjugated chromophores),[31–34] Al-based,[35] and 3d metal-based photosensitizers.[36–39] Among these, organic photosensitizers have gained significant attention due to their strong light absorption, high fluorescence quantum yields, and extended excited-state lifetimes, making them promising substitutes for noble-metal-based PSs.

Copper(I)-based photosensitizers (Cu-PSs) have gained prominence owing to their excellent photophysical properties and high earth abundance. The $d^{10}$ configuration of Cu(I) prevents metal-centred excited states, resulting in strong luminescence and long-lived excited states.[40] Ishitani and co-workers demonstrated that binuclear heteroleptic Cu(I) photosensitizers exhibit significantly extended excited-state lifetimes (>10 μs) and greater oxidative power than their mononuclear homoleptic analogues.[41] In parallel, Dey and co-workers reported that secondary coordination sphere interactions in an Fe-based molecular catalyst enabled selective electrochemical conversion of CO to $CH_4$.[42] These studies emphasize the critical role of ligand design and secondary coordination effects in modulating catalytic activity and selectivity of $CO_2$ and CO reduction.

This study explores a Ni-based molecular catalyst strategically designed to assess the influence of a pendant second-sphere amine group on the electrochemical and photochemical reduction of both $CO_2$ and CO to $CH_4$. A Ni-based complex (**C1**) was synthesized using two equivalents of the redox-active ligand 6-amino-2(phenylazo)pyridine) [**apap**], incorporating amine functionalities in the secondary coordination sphere. To systematically investigate its role, two additional Ni-based

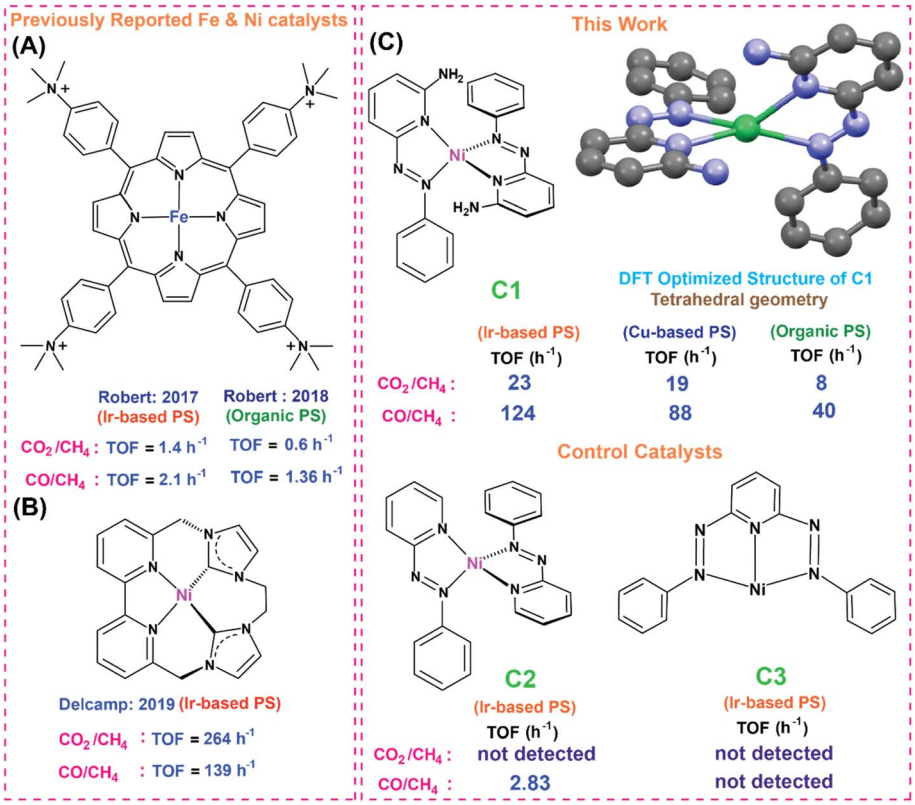


Fig. 1 (A) Reported mononuclear Fe catalysts for the photochemical $CO_2$/CO reduction reaction to $CH_4$. (B) Reported mononuclear Ni-based catalyst for the photochemical $CO_2$/CO reduction reaction to $CH_4$. (C) Present work: redox-active ligand-based Ni-catalysts **C1**: Ni-(**apap**)$_2$, **C2**: Ni-(**pap**)$_2$, and **C3**: Ni-(**dipap**)$_2$.

catalysts, **C2** and **C3**, were synthesized, lacking a pendant second-sphere amine group but retaining similar primary coordination geometries. Photocatalytic $CO_2$ reduction reactions were conducted in $CO_2$-saturated organic solvents under visible light irradiation (440 nm), while probing a range of combinations of sacrificial electron donors, proton sources, and photosensitizers (PSs). The study evaluated a diverse range of photosensitizers, including Ir-based (**Ir-PS-1** and **Ir-PS-2**), organic (**Cz-IPN**), and newly developed **PN(H)N** ligand-containing binuclear Cu(I) PSs with varying halogen bridges (Cl: **Cu-PS-1**, Br: **Cu-PS-2**, and I: **Cu-PS-3**). Notably, **Cu-PS-1** emerged as a highly stable and efficient photosensitizer, demonstrating superior TONs compared to the organic PS and serving as a promising cost-effective alternative to Ir-based PSs. It achieved the highest activity under the optimized conditions with $TON_{CO_2\rightarrow CO}$ (4789), $TON_{CO_2\rightarrow CH_4}$ (1130) and $TON_{CO\rightarrow CH_4}$ (3102), closely following the performance of **Ir-PS-1** ($TON_{CO_2\rightarrow CO}$ 6323, TON $_{CO_2\rightarrow CH_4}$ 1462 and $TON_{CO\rightarrow CH_4}$ (3897). However, **Cu-PS-3** exhibited a gradual decline in photocatalytic activity after 30 hours of continuous irradiation, eventually becoming inactive under prolonged light exposure. This deactivation is attributed to the dissociation of the dimeric species and the concurrent formation of a catalytically inactive Cu(II) state. Overall, this study demonstrates that strategic ligand design and effective metal–ligand cooperativity are key factors in enabling selective and efficient $CH_4$ production from $CO_2$ using earth-abundant metal catalysts. The catalytic systems exhibit consistent performance across a variety of photosensitizers and photochemical conditions, underscoring their potential applicability in solar fuel generation.

## Results and discussion

To explore the influence of a redox-active ligand in photocatalytic $CO_2$ to $CH_4$ conversion, a nickel-based complex (**C1**) was synthesized, incorporating two (6-amino-2(phenylazo) pyridine) [**apap**] ligands. The previously reported **apap** ligand was strategically selected due to its electron-rich azo functionality, which promotes efficient intramolecular charge transfer.[43] Additionally, the presence of a free pendant second-sphere amine moiety enables effective proton relay, contributing to enhanced catalytic performance.[43,44] The synthesis of **C1** followed a one-step coordination strategy, where the yellow **apap** ligand was dissolved in dichloromethane (DCM) and treated with 0.5 equivalent $Ni(ClO_4)_2\cdot 6H_2O$ in a mixture of acetonitrile (ACN) and DCM. To further investigate the role of the pendant second-sphere amine group, two additional Ni-based complexes, **C2** and **C3**, were synthesized using [**pap**][43] (2 equivalent) and [**dipap**][45] ligands (1 equivalent), respectively, where the a pendant second-sphere amine functionality is absent in both. The successful formation of all three complexes was initially confirmed by mass spectrometry, with the resulting isotopic patterns aligning well with theoretical predictions (Fig. S1), and CNH analysis further confirmed the bulk purity of all three complexes (Fig. S2–S4). Additionally, the complexes exhibited good solubility in polar aprotic solvents, such as dimethyl formamide (DMF), dimethyl sulfoxide (DMSO), and dimethyl acetamide (DMA), facilitating further spectroscopic studies. The preliminary optical study of the complexes was executed in DMA, where three distinct absorbance bands were observed between 190 and 1000 nm. To determine the origin of these transitions, optical spectra were acquired for the free [**apap**] ligand. This ligand exhibited a π–π* transition around 300 nm ($\varepsilon = 5615\ M^{-1}\ cm^{-1}$) (Fig. S5). In contrast, the complex **C1** showcased two peaks around 285 nm ($\varepsilon = 5520\ M^{-1}\ cm^{-1}$) and 306 nm ($\varepsilon = 5488\ M^{-1}\ cm^{-1}$), which appear as a splitting of the ∼300 nm peak observed in the ligand, presumably due to the lowering of symmetry (Fig. S5). Moreover, the free ligand exhibited a peak at ∼400 nm for an n–π* transition, while the complex showcased a strong broad band at ∼450 nm ($\varepsilon = 5505\ M^{-1}\ cm^{-1}$). This band at ∼430 nm is assigned to an overlap between ligand-based n–π* and [**apap**] → Ni(II) charge transfer transition (LMCT). The comparative FTIR spectra (Fig. S6A) of the free **apap** ligand and the **C1** complex displayed a subtle difference in the 3200–3500 $cm^{-1}$ region. Here, the distinct N–H stretching and bending modes of the free ligand disappeared in the **C1** complex, indicating Ni–N coordination along with possible hydrogen-bonding interactions.[44] Next, to find out the electronic structure of the distorted tetrahedral Ni(II) complex X-band EPR measurements of the distorted tetrahedral Ni(II) complex were carried out at 77 K, where no signal was observed (Fig. S6B). This behaviour is typical of high-spin Ni(II) ($d^8$, $S = 1$) complexes, particularly those with low-symmetry geometries such as distorted tetrahedral coordination. In such cases, strong zero-field splitting (ZFS) often occurs, which can shift the EPR transitions outside the detectable range or cause significant line broadening, making the signal difficult to observe. Furthermore, fast relaxation processes and low population differences between spin states at 77 K may also suppress the EPR signal. Nevertheless, DFT calculations confirm a high-spin state ($S = 1$) for the Ni(II) centre, supporting its paramagnetic nature (Fig. S7). The lack of an experimental EPR signal is therefore attributed to ZFS and relaxation effects rather than the absence of unpaired electrons.[46–52]

To investigate the role of photosensitizers (PS) in photochemical $CO_2$ reduction, a series of Ir- and Cu-based PSs were synthesized and characterized. The Ir-based photosensitizer **Ir-PS-1** was synthesized following a previously reported procedure.[44] The three Cu(I)-based photosensitizers (**Cu-PS-1**, **Cu-PS-2**, and **Cu-PS-3**) were synthesized as described in our recent report (Scheme S1).[53] Furthermore, the purity and structural integrity of the synthesized photosensitizers were confirmed by $^1H$, $^{13}C$, and $^{31}P$ NMR spectroscopy (Fig. S8–S16).[54] The optical spectra of all the Cu-PSs displayed a mixed π–π* and n–π* broad transition at ∼320–∼455 nm in DMA solvent (Fig. S17). To gain deeper insight into the oxidation state and electronic properties, EPR and cyclic voltammetry (CV) studies were performed. The EPR silence of **Cu-PS-1**, **Cu-PS-2**, and **Cu-PS-3** confirmed that Cu remained in the +1 oxidation state, consistent with its $d^{10}$ electronic configuration represented by a dotted line (Fig. 3A). Redox behavior was further examined through CV analysis, which revealed distinct Cu(I)/Cu(0) reduction potentials at −1.3 V (**Cu-PS-1**), −1.6 V (**Cu-PS-2**), and −1.7 V (**Cu-PS-3**) *vs.* $FeCp_2^{+/0}$ (Fig. S18). The increasing negative shift in redox

potential correlated with the influence of the halide ligands, where Cu–I exhibited the weakest electron affinity, followed by Cu–Br and Cu–Cl, indicating a tunable electronic environment. These findings establish that the Cu–PS complexes are promising alternatives to Ir-based photosensitizers for photochemical $CO_2$ reduction.

### Electrocatalytic $CO_2$RR

After the preparation of the catalyst **C1**, the redox properties of the catalyst were examined by cyclic voltammetry in DMA media, with all the measured potentials reported against the ferrocenium/ferrocene ($FeCp_2^{+/0}$) redox couple. During a cathodic scan ranging from 0.12 V to −2.3 V, **C1** exhibited four electrochemical responses at −0.7 V, −1.35 V, −1.5 V, and −1.8 V under an argon atmosphere (Fig. 3B and S19). Among these signals, the first response at −0.7 V is assigned to the $Ni^{II/I}$ redox process,[21,55,56] while the remaining three signals correspond to ligand-centred redox processes, as confirmed by comparison with a previously reported Zn analogue.[66] To further validate these assignments, *in situ* spectroelectrochemical optical studies were performed. The emergence of a new peak around 600 nm (under an applied potential of −0.9 V), coupled with the reduction of a peak near 450 nm, confirms the transition from $Ni^{II}$ to $Ni^{I}$ (Fig. S20).[57] The formation of Ni(I) was further corroborated by EPR spectroscopy, where a rhombic signal was observed with four different *g*-values ($g_1 = 2.12$, $g_2 = 2.02$, and $g_3 = 1.976$, and $g_4 = 1.93$) (Fig. S21A).[58–60] Additionally, to investigate the ligand-based contribution to the second peak, a similar EPR experiment was conducted at an applied potential of −1.3 V. The resulting spectrum, which shows a *g*-value of 2.001 along with additional *g*-values ($g_1 = 2.12$, $g_2 = 2.02$, and $g_4 = 1.93$) (Fig. S21B), indicates the formation of a radical species along with the Ni(I) state.[58,59,61] Moreover, to corroborate these experimental results, electronic structure calculations were performed. The first one-electron reduction is metal-centred, reducing Ni(II) to Ni(I), as confirmed by molecular orbital (MO) analysis, matching the spin density ($S = 1/2$) observed in EPR data ($\langle g \rangle = 2.1$, $\Delta g = 0.58$) (Fig. S21). The second reduction is ligand-centred, supported by MO/spin density analysis and elongation of the N=N bond to 1.333 Å, indicating the formation of Ni(I)–$L^{\bullet-}$ (Fig. S22). The resulting doubly reduced intermediate Ni(I)–$L^{\bullet-}$ in Fig. S22 adopts a triplet state ($S = 1$), which is energetically favoured over the singlet species by 0.6 kcal $mol^{-1}$. The unpaired electrons are distributed between the metal centre and the ligand. This is corroborated by EPR features ($\langle g \rangle = 2.076$, $\Delta g = 0.58$; Fig. S21B), confirming contributions from both centres. Upon introducing $CO_2$, a sharp increase in reductive current was observed starting at −1.4 V *vs.* $FeCp_2^{+/0}$, coinciding with the first ligand reduction peak (Fig. 3B). Upon addition of phenol (PhOH) as an external proton source, the reductive signal increased slightly, consistent with the involvement of proton-coupled electron transfer (PCET) during $CO_2$ activation (Fig. S19). Hence, these CV experiments underline the inherent activity of the **C1** complex for electrochemical $CO_2$ reduction. To assess catalytic activity and product distribution, bulk electrolysis was carried out under $CO_2$-saturated DMA with phenol as the proton source at −1.6 V (Fig. S23). Gas chromatography of the electrochemical cell headspace, following the electrolysis, confirmed the generation of CO and $H_2$ during electrocatalysis, affording $TON_{CO} \approx 19$ (Fig. S24A). In contrast, in the absence of a proton source, CO production decreased to $TON_{CO} \approx 12$, underscoring the importance of proton donors in facilitating $CO_2$ reduction. To further assess the reactivity of **C1** toward CO activation, CV experiments were performed under 1 atm CO in DMA. A distinct reductive wave at −1.25 V was observed, which intensified upon addition of phenol, indicating enhanced CO reduction (Fig. 3B and S19). Bulk electrolysis of **C1** under CO-saturated DMA with phenol at −1.5 V *vs.* $FeCp_2^{+/0}$ (Fig. S23) yielded $CH_4$ and $H_2$ as gaseous products, with $TON_{CH_4} \approx 16$. In the absence of phenol, $CH_4$ formation was markedly lower ($TON_{CH_4} \approx 9$), confirming the critical role of proton transfer in enabling multi-electron CO reduction to $CH_4$. Electrochemical evaluation of **C2** and **C3** revealed increased current densities under $CO_2$ compared to Ar, with onset potentials of −1.45 V (**C2**) and −1.48 V (**C3**), suggesting $CO_2$RR activity (Fig. S25 and S26). However, bulk electrolysis produced only modest amounts of CO ($TON_{CO} \approx 6$ for **C2**; ≈2 for **C3**), and phenol addition had no measurable effect on product distribution. Together, these results highlight the unique contribution of the pendant amine group in **C1**, which likely engages in proton-coupled electron transfer (PCET) to stabilize reduced Ni intermediates and promote selective $CO_2$RR. The absence of this feature in **C2** and **C3** correlates with diminished activity and efficiency. While **C1** exhibits intrinsic competence for $CO_2$ and CO reduction, its comparatively modest turnover under electrochemical conditions suggests that the distinct reaction environment under photocatalytic conditions, including the reducing power of the photosensitizer, proton availability, and PCET processes, plays an important role in promoting selective CO and $CH_4$ production.

### Photocatalytic $CO_2$RR

Building on the electrochemical $CO_2$ reduction studies, the photocatalytic performance of **C1** was evaluated under visible-light irradiation in $CO_2$-saturated, proton-enriched DMA solvent using BIH with 10% v/v TEOA as the sacrificial electron donor (SED). A series of photosensitizers (PSs) were systematically screened, including **Ir-PS-1**, **Ir-PS-2**, **CzIPN**, and the Cu(I)-based dimers **Cu-PS-1**, **Cu-PS-2**, and **Cu-PS-3** (Fig. 2). Prior to photocatalytic testing, cyclic voltammetry and optical spectroscopy were employed to establish the redox potentials and absorption profiles of the PSs (Fig. S27–S29). Fluorescence quenching experiments were subsequently performed to probe excited-state electron transfer processes. BIH efficiently quenched the steady-state photoluminescence (PL) of all PSs (Fig. 4 and S30–S32), confirming rapid photoinduced electron transfer from BIH to the excited PS. In contrast, incremental addition of **C1** produced negligible quenching of PL intensity (Fig. 4, S33 and S34). These results rule out direct excited-state energy or electron transfer from the PS to **C1**. Instead, the data support a mechanism in which the reduced PS, generated by reductive quenching with BIH, serves as the effective electron donor to **C1**, thereby initiating the photocatalytic $CO_2$ reduction cycle.

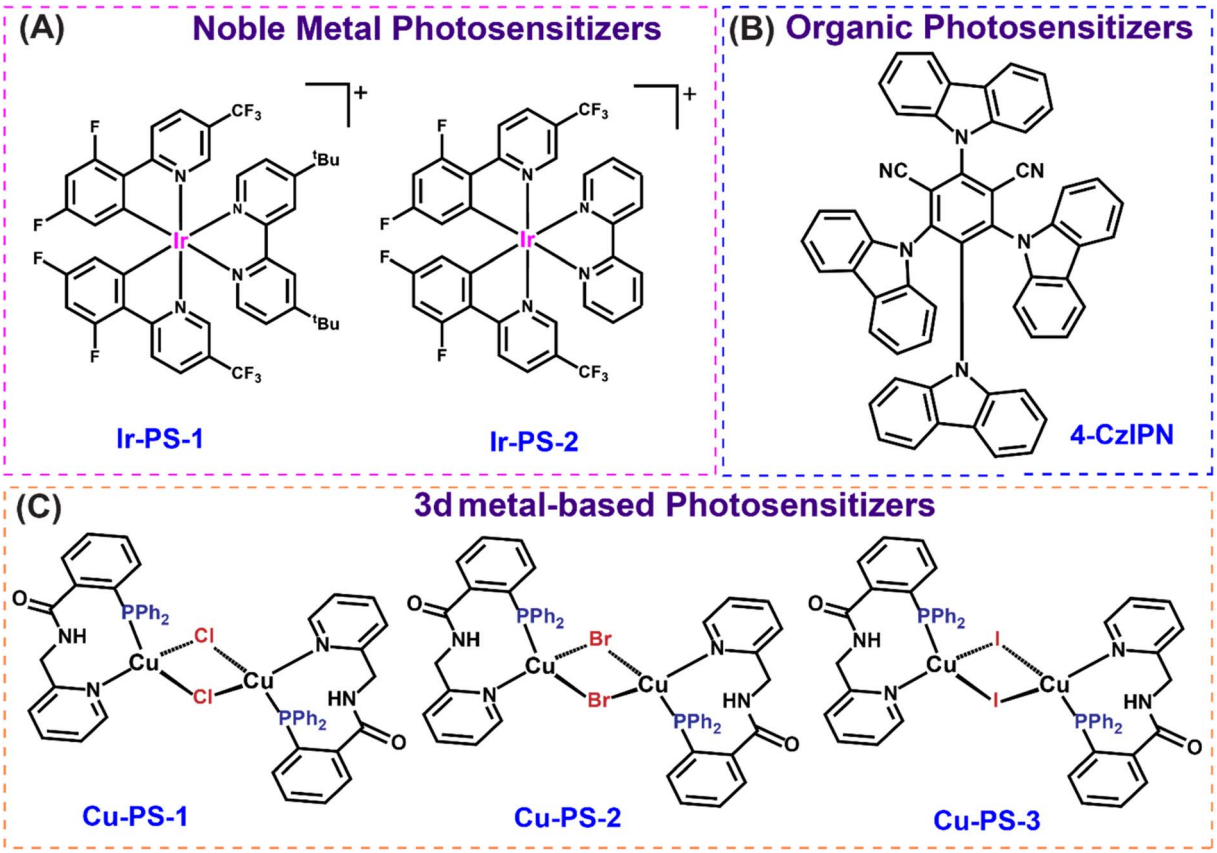


Fig. 2 (A) Noble-metal Ir-based catalysts: $[Ir\{dF(CF_3)ppy\}_2(bpy)]^+$ and $[Ir\{dF(CF_3)ppy\}_2(dtbbpy)]^+$, (B) organic photosensitizers: 4-**CzIPN** (1,2,3,5-tetrakis(carbazol-9-yl)-4,6-dicyanobenzene), and (C) 3d metal-based $Cu^I$ catalysts, $[(CuCl)_2\{PN(H)N\}_2\text{-}\kappa^2\text{-}P,N]$, $[(CuBr)_2\{PN(H)N\}_2\text{-}\kappa^2\text{-}P,N]$ and $[(CuI)_2\{PN(H)N\}_2\text{-}\kappa^2\text{-}P,N]$.

### Optimized photocatalytic conditions and selectivity

Photochemical $CO_2$ reduction experiments were performed in a gas-tight quartz vessel under monochromatic 440 nm irradiation and systematically optimized by varying the PS, SED, proton source, and other parameters (Table S1). Gaseous products were analyzed by gas chromatography, while the liquid phase was probed using ion chromatography and NMR spectroscopy. The dominant products were CO and $CH_4$, with only trace $H_2$ observed; no liquid products were detected. Under optimized conditions with **Ir-PS-1**, **C1** produced CO with a TON of 6323 after 32 h of irradiation (Fig. 4A, S35 and Table S1, entry 8). Intriguingly, prolonged irradiation led to a gradual decline in CO formation accompanied by increased $CH_4$ production, reaching a TON of 1462 after 68 h with a TOF of 22 $h^{-1}$ (Fig. 4C and S35–S37). This temporal shift highlights the ability of **C1** to mediate deeper $CO_2$ reduction, expanding the reduction cycle from CO to $CH_4$. The addition of an external proton source significantly enhanced activity (Table S1, entry 1 *vs.* entry 8), underscoring the role of the pendant $–NH_2$ group in facilitating proton relay. Systematic variation of phenol concentration revealed that CO production peaked at 0.12 mM (Fig. S38A). At higher concentrations, CO turnover declined while $H_2$ generation increased, reflecting competitive proton reduction. $CH_4$ formation exhibited a stronger dependence on proton concentration relative to CO, consistent with its more demanding $8e^-/8H^+$ pathway *versus* the $2e^-/2H^+$ requirement for CO formation. Together, these results establish that proton availability critically governs product selectivity, while the $–NH_2$ group within **C1** promotes intramolecular hydrogen bonding and accelerates PCET processes. At excessive proton loadings, this advantage shifts toward parasitic $H_2$ evolution, revealing a delicate balance between proton concentration and selective $CO_2$-to-CO/$CH_4$ conversion.

### Comparison with C2 and C3 and the critical role of the $–NH_2$ group

To delineate the role of the a pendant second-sphere amine ($–NH_2$) group in secondary coordination sphere interactions, photocatalytic $CO_2$ reduction was evaluated with **C2** and **C3** under conditions identical to those used for **C1**. In sharp contrast, both **C2** and **C3** selectively generated CO, with TON values of 2758 (**C2**, 68 h) and 2251 (**C3**, 68 h) (Table S1, entries 24 and 28 and Fig. S39–S40). Importantly, variation in proton source concentration produced no measurable effect on CO output (Fig. S38 *vs.* S41), confirming the inability of these catalysts to access deeper reduction pathways beyond CO formation. This divergence highlights the critical function of the pendant $–NH_2$ group in **C1**. Its presence not only enhanced

$CO_2$-to-CO turnover (~5-fold higher TON compared to **C2** and **C3**) but also uniquely enabled $CH_4$ production, a transformation absent in the control complexes. The ability of **C1** to engage in PCET *via* intramolecular proton relay appears decisive in lowering barriers for multi-electron reduction beyond the $2e^-/2H^+$ step. These findings firmly establish **C1** as a selective and efficient photocatalyst, with secondary coordination sphere engineering serving as a powerful lever for tuning product distribution. Achieving visible-light-driven $CO_2$-to-$CH_4$ conversion, a rare outcome for molecular 3d-metal catalysts, demonstrates the potential of rational ligand design in orchestrating complex multi-electron photochemical processes. Moreover, the pronounced dependence of product selectivity on proton availability provides guiding principles for the design of next-generation photocatalysts aimed at efficient solar-to-fuel conversion. Building on this foundation, the system was next examined with organic and 3d-metal-based photosensitizers (PSs) to eliminate reliance on noble-metal PSs. In the presence of **CzIPN**, **C1** exhibited CO production with a TON of 3634 after 32 h (Table S1, entry 11, Fig. 4A and S42). As observed with Ir-based systems, CO turnover decreased over time, while $CH_4$ formation increased, reaching $TON_{CH_4} \approx 498$ after 68 h (Fig. 4B and S42). Although organic PSs such as **CzIPN** provide a cost-effective alternative to noble-metal-based PSs, their moderate catalytic activity and limited photostability remain major drawbacks, motivating the exploration of 3d-metal-based PSs.

### Copper photosensitizer-performance and selectivity

Three dimeric Cu(I) PSs (**Cu-PS-1**, **Cu-PS-2**, and **Cu-PS-3**) bearing halogen bridges (Cl, Br, and I) were evaluated for $CO_2$RR. **Cu-PS-1** showed the highest activity, producing CO with TON ≈ 4789 (Table S1, entry 12, Fig. 4A and S43) and $CH_4$ with TON ≈ 1130 after 68 h (Fig. 4B and S43). **Cu-PS-2** produced CO with TON ≈ 4007 and $CH_4$ with TON ≈ 642 (Table S1, entry 13, Fig. 4A, B and S44), whereas **Cu-PS-3** was significantly less active ($TON_{CO}$ ≈ 2579; $TON_{CH_4}$ ≈ 364) (Table S1, entry 16, Fig. 4A, B and S45). Notably, **Cu-PS-2** and **Cu-PS-3** deactivated after 62 h and 42 h, respectively, accompanied by visible solution colour changes, while **Cu-PS-1** retained activity beyond 68 h without degradation.

### Mechanistic insights into Cu(I) PS deactivation

*In situ* EPR, $^1$H NMR, and $^{31}P\{^1H\}$ NMR revealed progressive conversion of $Cu^I$–X–$Cu^I$ dimers (X = I, Br) to Cu(II) species during extended irradiation, particularly for **Cu-PS-3**. Broadening and disappearance of NMR signals (Fig. S46–S53) and the emergence of paramagnetic EPR features ($g \approx 2.1$, hyperfine splitting for $I = 3/2$; Fig. 3A) confirmed Cu(I) → Cu(II) oxidation. Fluorescence quenching studies further demonstrated the loss of excited-state activity after 62 h (Fig. S32B and S54). DFT calculations provided a mechanistic basis, showing that weaker orbital overlap and lower-lying antibonding orbitals in **Cu-PS-3** facilitate Cu–I bond cleavage upon photoexcitation, triggering deactivation. Among the three Cu(I)-based dimeric photosensitizers (PSs), the Cu–halogen bond strength follows the trend: Cu–Cl–Cu ≫ Cu–Br–Cu > Cu–I–Cu. This is attributed to the poor orbital overlap between the Cu 3d orbital and the larger, more diffuse valence p orbital of iodine, as well as the lower-lying lowest unoccupied molecular orbital (LUMO or antibonding orbital) of **Cu-PS-3**, as revealed by DFT calculations. Upon photoirradiation, electron excitation into this antibonding orbital leads to cleavage of the Cu–I–Cu bridging bond. Consequently, the Cu(I) centre is oxidized to Cu(II), resulting in the loss of photosensitizer properties and termination of $CO_2$ reduction activity. This deactivation pathway is supported by EPR spectroscopy (Fig. S55). It was previously discussed that the lifetime of triplet excited states of Cu(I) systems, having a $d^{10}$ configuration, is much longer than that of Cu(II) systems. Hence, Cu(I) acts as a photosensitizer. These findings establish **Cu-PS-1** as the most efficient and stable photosensitizer, maintaining long-term catalytic activity without significant structural degradation. In contrast, **Cu-PS-3** deactivates due to Cu(I) → Cu(II) conversion, triggered by weak Cu–I bonds and LUMO-mediated bond cleavage. The combined EPR, NMR,

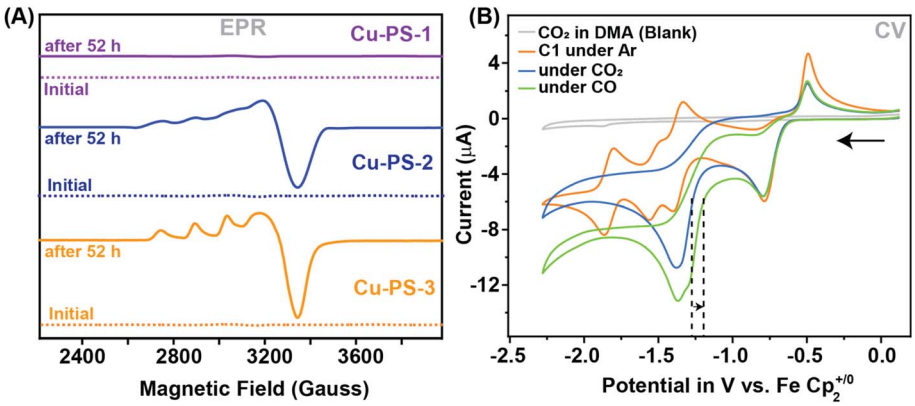


Fig. 3 (A) The experimental EPR spectrum recorded initially (dotted lines) and after 52 h (solid lines) of light irradiation for all the $Cu^I$-PS, $Cu^I$-PS-1 (violet trace), $Cu^I$-PS-2 (blue trace), $Cu^I$-PS-3 (orange trace) photosensitizers recorded in DMA at 77 K without photoirradiation. (B) Comparative cyclic voltammograms (CVs) of blank DMA (without a catalyst) solvent under a $CO_2$-saturated atmosphere (grey trace) and 0.5 mM **C1** under Ar (orange trace), $CO_2$ (blue trace), and CO (green trace) atmospheres. All the data were recorded in DMA in the presence of 0.1 M $nBu_4N^+BF_4^-$ electrolyte at a 0.1 V per s scan rate. The horizontal arrows signify the initial scan direction.

fluorescence, and DFT results highlight fundamental structure–stability relationships and provide design principles for next-generation Cu-based photosensitizers for sustainable $CO_2$RR.

### Photocatalytic CO reduction reaction (CORR)

During extended photochemical $CO_2$ reduction (>32 h), a striking shift in product selectivity was observed: *in situ*-generated CO was progressively consumed and converted into $CH_4$. This observation motivated a direct evaluation of photocatalytic CO reduction (CORR) under otherwise identical conditions, substituting CO for $CO_2$ as the feedstock. Remarkably, $CH_4$ formation was significantly enhanced, with $TON_{CH_4}$ values substantially exceeding those obtained under $CO_2$-saturated conditions. After 30 h of irradiation, $TON_{CH_4}$ values reached 3897 (**Ir-PS-1**), 3685 (**Ir-PS-2**), 1250 (**CzIPN**), 3102 (**Cu-PS-1**), 1587 (**Cu-PS-2**), and 784 (**Cu-PS-3**) (Table S1, entries 18–26, Fig. 4C, D and S56). These results correspond to an approximate twofold increase in $CH_4$ production relative to $CO_2$RR, strongly implicating CO as a more reactive intermediate. Because CO requires fewer proton–electron equivalents for full reduction to $CH_4$, CORR emerges as the more favourable pathway under photochemical conditions. Given the expected involvement of proton-coupled electron transfer (PCET) during CO hydrogenation, the effect of proton source concentration was systematically probed using **Ir-PS-1**. An optimal concentration of phenol (PhOH) increased $TON_{CO\rightarrow CH_4}$ by ∼30% compared to reactions without an added proton donor (Table S1, entries 15 *vs.* 16 and Fig. S41). However, excessive protonation promoted parasitic hydrogen evolution (HER), evidenced by an increase in $H_2$ production (Fig. S40 and S41), underscoring the delicate balance of proton availability required for selective $6H^+/6e^-$ conversion of CO to $CH_4$. Finally, to confirm that methane originated exclusively from the $CO_2$ reduction pathway, isotope-labelling experiments were conducted with $^{13}CO_2$. Gas chromatography–mass spectrometry (GC–MS) analysis of the headspace products revealed the characteristic $m/z = 17$ signal for $^{13}CH_4$, unambiguously verifying that $CH_4$ formation derived solely from the introduced $CO_2$ feedstock (Fig. S57–S59). To further probe the importance of ligand effects in PCET, photochemical CO reduction experiments were conducted with **C2** and **C3**, which lack the secondary $-NH_2$ functional group present in **C1**. Strikingly, while **C2** facilitated $CH_4$ formation with a $TON_{CH_4}$ of 88 after 32 hours (Table S1; entries 25–30), **C3** exhibited no activity for CO to $CH_4$ conversion even in the presence of 0.6 mM phenol as a proton source, confirming that the a pendant second-sphere amine group plays a pivotal role in facilitating proton transfer during CORR. This result aligns with previous $CO_2$RR findings, further demonstrating that rational ligand design incorporating proton relays is essential for achieving selective multi-electron $CO_2$ and CO reduction to $CH_4$.

### Mechanistic insight for electrochemical $CO_2$/CO to $CH_4$ conversion *via in situ* spectroscopic studies

**C1** operates as a dual active catalyst for the transformation of $CO_2$ and CO to $CH_4$, functioning under both electrochemical and photocatalytic conditions. Under photochemical conditions, $CO_2$ is converted to $CH_4$, whereas under electrochemical conditions, $CH_4$ formation proceeds through a stepwise pathway involving CO intermediates. In this work, a comprehensive mechanistic framework for the $CO_2$ to $CH_4$ conversion is advanced, supported by *in situ* spectroscopic analyses and corroborated by DFT calculations. A combination of EPR, FTIR, and UV-vis spectroscopy was employed to monitor reaction intermediates under controlled $CO_2$ and CO atmospheres. Complementary DFT studies elucidated the critical role of the pendant second-sphere amine ($-NH_2$) group, which stabilizes $CO_2$- and CO-bound intermediates through hydrogen bonding interactions. The catalytic cycle commences with the stepwise two-electron reduction of [Ni II(L)$_2$] to the catalytically active [LNi(I)–L$^{\bullet-}$] species **3** (Fig. 6). The formation of species **3** was established through *in situ* spectroscopic experiments and supported by DFT analysis (Fig. S21 and S22). Upon exposure to $CO_2$, nucleophilic attack by **3** on the electrophilic carbon centre of $CO_2$ yields a $CO_2$ adduct (species **4**). Protonation of this intermediate generates a Ni–COOH species (**5**), identified by the appearance of a new FTIR band at 1652 cm$^{-1}$, attributable to the C═O stretch of the Ni-bound COOH moiety (Fig. S60). Additional vibrational features at 2100 cm$^{-1}$ and 1962 cm$^{-1}$ confirmed the presence of Ni–CO and free CO, respectively (Fig. 5A).[62] To substantiate these assignments beyond qualitative vibrational analysis, isotopic labelling experiments using $^{13}CO_2$ were performed. Upon replacing $^{12}CO_2$ with $^{13}CO_2$, the CO stretching vibration shifts from 1962 cm$^{-1}$ to 1911 cm$^{-1}$ for the Ni–CO adduct (Fig. S60), and the COOH-related band shifts from 1652 cm$^{-1}$ for Ni(II)–$^{12}$COOH to 1598 cm$^{-1}$ for the corresponding lower-frequency $^{13}$COOH analogue, consistent with the expected isotopic mass effect (Fig. 5C). These FTIR spectra were recorded under identical conditions at a catalyst concentration of 30 mM, with the $^{12}CO_2$-derived (pink) and $^{13}CO_2$-derived (green) adducts showing clear, systematic isotope-dependent shifts. To further validate formation of the Ni–CO intermediate (**6**), *in situ* FTIR studies were performed under CO-saturated conditions, revealing a progressive increase in the 1950 cm$^{-1}$ band, consistent with accumulation of Ni–CO species (Fig. 5B). This conclusion was reinforced by control EPR experiments, wherein exposure of Ni$^{I}$ (**2**) to CO yielded a distinct spectrum diagnostic of Ni–CO formation (species **6**). Once generated, species **6** can either release CO, regenerating the catalyst ($CO_2$ to CO pathway), or undergo further reduction *via* a $6H^+/6e^-$ sequential route to $CH_4$ (CO to $CH_4$ pathway; Fig. S24B). The pendant second-sphere amine group plays a pivotal role at this stage, providing a proton relay network that lowers the barrier for CO protonation and facilitates multi-electron reduction. In its absence, as in catalysts **C2** and **C3**, $CH_4$ formation is markedly suppressed. Stepwise $CH_4$ evolution proceeds from Ni–CO species **6** through successive two-electron reductions, affording the reduced intermediate **7** (Fig. 6). Species 7 engages in a proton-coupled electron transfer (PCET) sequence, mediated by $-NH_2$ interactions, to form intermediate **8**. Subsequent PCET steps traverse intermediates **9** and **10**, culminating in the formation of a $CH_3$-bound Ni$^{III}$ species (**11**), in the catalytic cycle.[58,63] DFT calculations were used to

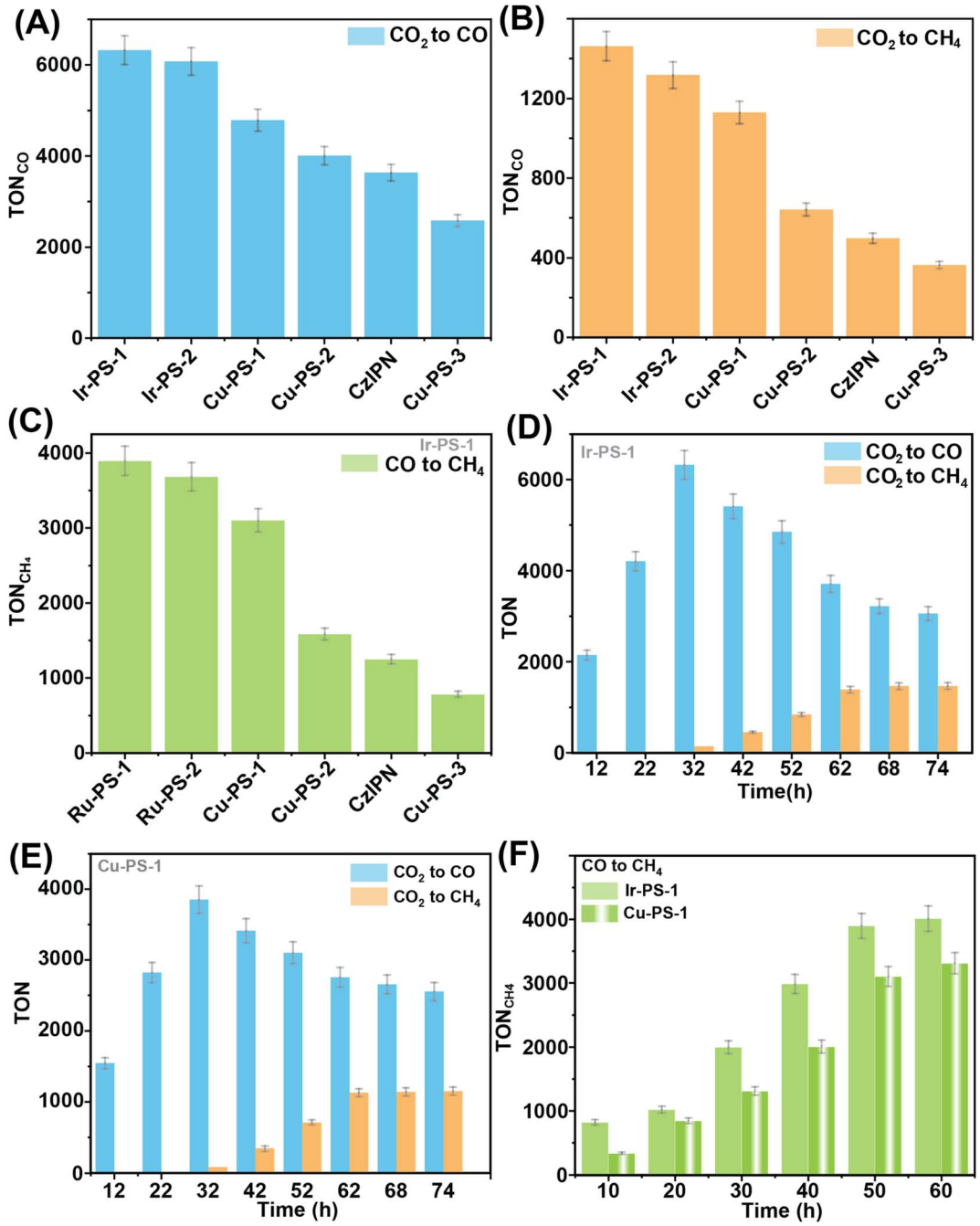


Fig. 4 (A) Progress of photocatalytic $CO_2$ to CO conversion and (B) $CO_2$ to $CH_4$ conversion over time using individual photo-sensitizers **Ir-PS-1**, **Ir-PS-2**, **CzIPN**, **Cu-PS-1**, **Cu-PS-2**, and **Cu-PS-3** along with the catalyst **C1**, phenol as a proton source, and BIH as a sacrificial donor in a different photo-setup under 440 nm light irradiation under $CO_2$ saturated conditions. (C) Progress of photocatalytic CO to $CH_4$ conversion over time using individual photo-sensitizers **Ir-PS-1**, **Ir-PS-2**, **CzIPN**, **Cu-PS-1**, **Cu-PS-2**, and **Cu-PS-3** along with the catalyst **C1**, phenol as a proton source, and BIH as a sacrificial donor in a different photo-setup under 440 nm light irradiation under CO-saturated conditions. (D and E) The comparative progress of photocatalytic $CO_2$ to CO and $CH_4$ in terms of TON in the presence of (D) **Ir-PS-1** and (E) the 3d-metal-based PS, **Cu-PS-1** with the catalyst **C1**, phenol as a proton source, and BIH as a sacrificial donor in a different photo-setup under 440 nm light irradiation under $CO_2$ saturated conditions. (F) The comparative progress of photocatalytic CO to $CH_4$ in terms of TON in the presence of **Ir-PS-1** and the 3d-metal-based PS, **Cu-PS-1** with the catalyst **C1**, phenol as a proton source, and BIH as a sacrificial donor in a different photo-setup under 440 nm light irradiation under CO saturated conditions. All the photochemical experiments were carried out at 2 μM catalyst concentration in DMA (2 mL), BIH (0.2 M) as the electron donor, and photosensitizer (PS) (8 mM), irradiated with a 440 nm LED.

characterize the unstable intermediates **9** and **10**, while EPR spectroscopy provided direct evidence for intermediate **11**. Specifically, EPR spectra recorded under CO-saturated conditions at −1.5 V displayed a distinct signal attributable to $Ni^{III}$–$CH_3$ (**11**), distinct from previously observed species (Fig. S21E). Further validation came from chemical oxidation of

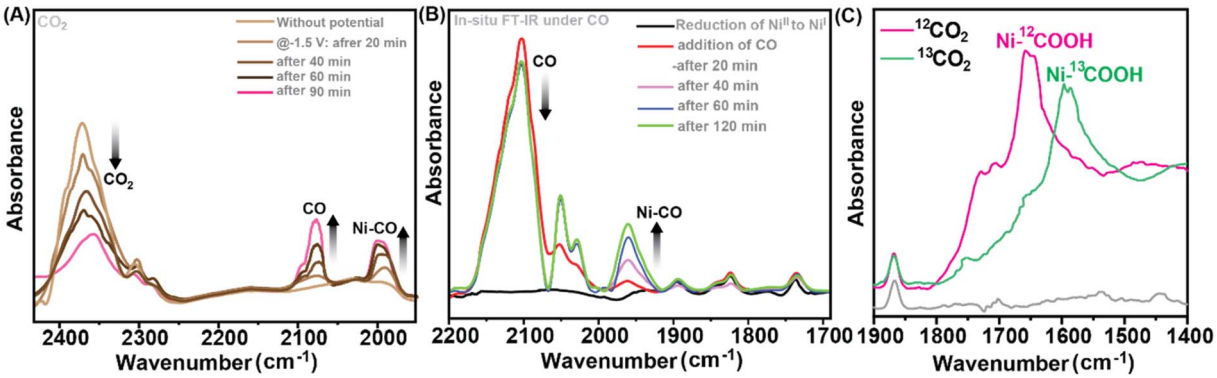


Fig. 5 (A) The gradual change in the FTIR spectra of the complex **C1** (30 mM) around the 2400–1900 $cm^{-1}$ region during a spectroelectrochemistry experiment in a 100% $CO_2$ atmosphere executed at −1.6 V *vs.* $FeCp_2^{+/0}$. The vertical arrows highlight the appearance of the $\bar{\nu}_{CO}$ signal and $\nu_{Ni-CO}$ signals, and simultaneous disappearance of $\bar{\nu}_{CO_2}$. (B) the *in situ* generation of the $\nu_{Ni-CO}$ signal through the purging of CO gas into the DMA solution of one electron-reduced species, $[Ni^{I}(\mathbf{pap})_2]$. (C) FTIR spectra of Ni(II)–$^{12}$COOH (1652 $cm^{-1}$) *vs.* Ni(II)–$^{13}$COOH (1598 $cm^{-1}$) adducts in solvent (catalyst concentration 30 mM). The pink spectra represent the $^{12}CO_2$ adducts of the catalyst **C1**, and the green ones represent its $^{13}CO_2$ adducts. All data were recorded in DMA media at 298 K temperature with a Pt-mesh working electrode, a Pt wire counter electrode, and a Ag microware pseudo-reference electrode assembled in an OTTLE cell.

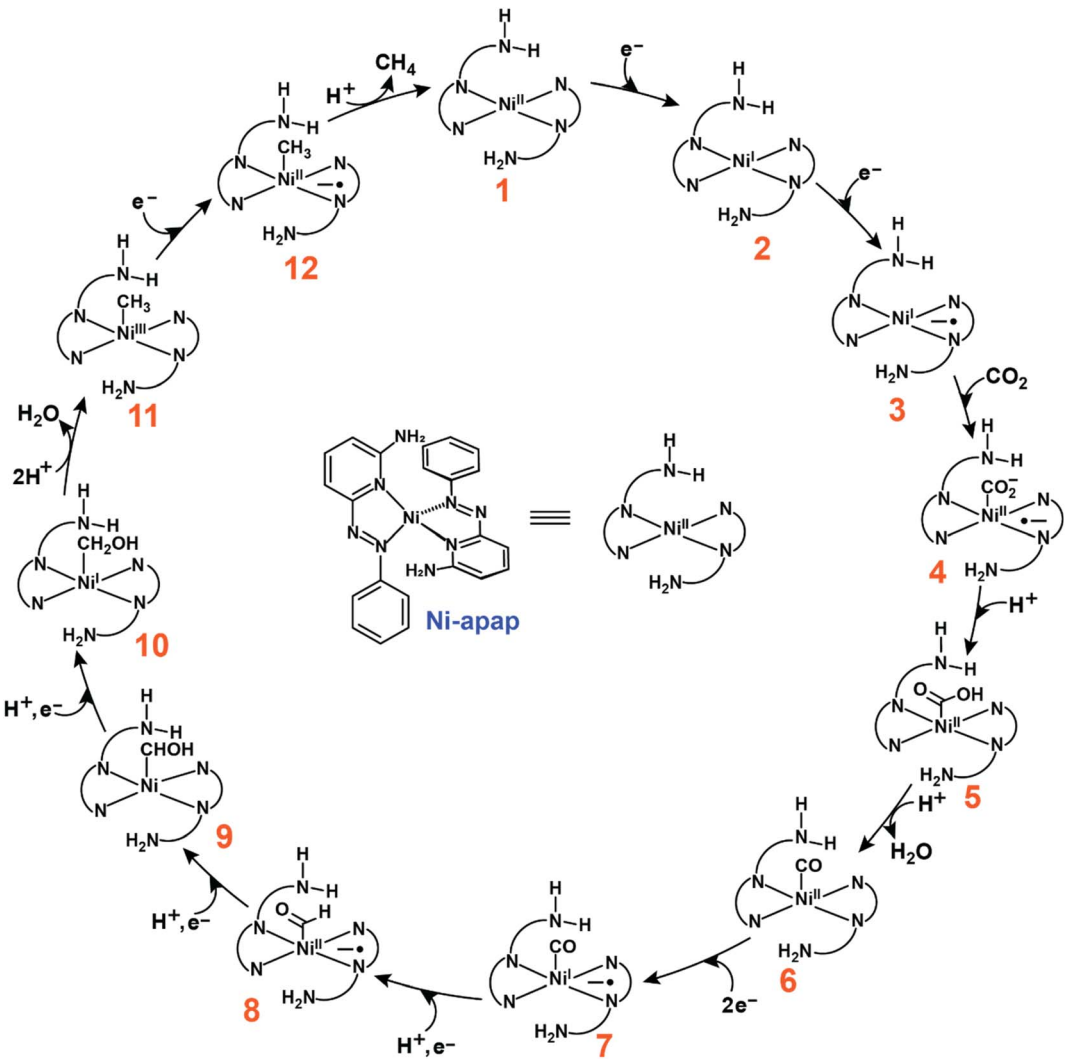


Fig. 6 A probable mechanistic pathway for $CO_2$ to $CH_4$ conversion.

$Ni^{II}$ to $Ni^{III}$ with ceric ammonium nitrate (CAN), affording an EPR spectrum in excellent agreement with that of species **11** (Fig. S21F).[58,63] To further validate the formation of the $CH_3$-bound Ni(III) intermediate under photochemical conditions, a series of key photochemical experiments were conducted in the presence of CO.[64–66] The experiments were performed in a gas-tight quartz vessel under monochromatic 440 nm visible light, employing BIH as an electron donor, **Ir-PS-1** as a photosensitizer, PhOH as a proton source, and 5 equivalents of $CH_3I$ under CO-saturated conditions. The gaseous and liquid products were monitored at different time intervals using gas chromatography (GC) and ion chromatography (IC), respectively. Initially, after 1 hour of irradiation, no detectable gaseous or liquid products were observed. However, after 3 hours, GC analysis revealed the formation of $CH_4$ and $C_2H_6$ as the sole gaseous products (Fig. S61). The production of $CH_4$ and $C_2H_6$ continued to increase over time, with a significant rise observed after 6 hours, while no liquid-phase products were detected throughout the experiment. To investigate the mechanistic pathway of $C_2H_6$ formation, particularly its potential generation *via* a radical-mediated reaction involving Ni–$CH_3$ and $CH_3I$, control experiments were conducted (Fig. S61). When the reaction was performed in the absence of the catalyst, neither $CH_4$ nor $C_2H_6$ was detected. In contrast, when $CH_3I$ was omitted, only $CH_4$ formation was observed, with no detectable $C_2H_6$. Collectively, these photochemical and electrochemical investigations provide compelling evidence that methane formation proceeds through the intermediate species **11** and **12**, supporting the proposed mechanistic framework.

As discussed earlier, fluorescence quenching studies were performed to investigate the photocatalytic mechanism involving **C1** using several photosensitizers, including Ir-based PSs, **CzIPN**, **Cu-PS-1**, **Cu-PS-2**, and **Cu-PS-3**. The addition of **C1** caused negligible changes in the fluorescence intensity of the photosensitizers, whereas BIH induced significant fluorescence quenching. These results indicate that the photocatalytic reaction proceeds *via* a reductive quenching pathway, where BIH reductively quenches the excited photosensitizer. To further elucidate the mechanistic details, optical spectroscopic studies were conducted in the presence of the **C1**, **Ir-PS-1**, and BIH under both Ar and $CO_2$ atmospheres with 440 nm light irradiation. The reaction is initiated by the photoexcitation of $[\mathbf{Ir\text{-}PS\text{-}1}]^+$, generating a mixed excited-state involving $^3$MLCT ($t_{2g} \rightarrow \pi^*_{N=N}$) and $^3$LC ($\pi_{C=N} \rightarrow \pi^*_{N=N}$) transitions. This excited state undergoes reductive quenching by BIH, resulting in the formation of $[\mathbf{Ir\text{-}PS\text{-}1}]^0$ and the oxidized form of BIH ($BIH^{\bullet+}$), which rapidly deprotonates to form $BI^{\bullet}$. The radical species $BI^{\bullet}$ is a highly reducing intermediate ($E_0(BI^{\bullet}/BI^+) = -2.06$ V *vs.* $FeCp_2^{+/0}$) and can subsequently reduce another molecule of $[\mathbf{Ir\text{-}PS\text{-}1}]^+$, yielding two equivalents of $[\mathbf{Ir\text{-}PS\text{-}1}]^0$ in the overall photoinduced process.[29,30,67,68] The reduced $[\mathbf{Ir\text{-}PS\text{-}1}]^0$ species serves as an electron donor to facilitate the stepwise reduction of **C1** and generate $[Ni^I(\mathbf{apap}^{\bullet-})]$. The appearance of a new absorption peak around 600 nm in the optical spectra recorded under an Ar atmosphere after 3 hours of light irradiation indicates the reduction of Ni(II) to Ni(I). This reduction was further corroborated by spectroelectrochemical studies, where a similar absorption feature emerged upon applying a potential of −0.95 V *vs.* $FeCp_2^{+/0}$. The consistency of this spectral signature under both photochemical (Fig. S62A) and electrochemical (Fig. S62B) conditions provides strong evidence that Ni(II) reduction to Ni(I) occurs *via* the reductive quenching of **Ir-PS-1**. Interestingly, under identical photocatalytic conditions in the presence of $CO_2$, the diminishing peak intensity around 600 nm, accompanied by the simultaneous emergence of a new peak in the 500–550 nm region, confirms the formation of a $CO_2$ adduct species. However, the CV studies under Ar *vs.* $CO_2$ and our previously reported Cu-based analogues depict the $CO_2$RR proceeding through a ligand-induced, metal-based pathway.[43] Upon light irradiation, similar to **Ir-PS-1**, **Cu-PS-1** undergoes photoexcitation to its triplet excited state, $^3[Cu^I\text{-PS}]^*$, which is subsequently quenched by BIH, forming an unstable reduced species. This reduced species then undergoes sequential electron transfer steps and converts $[Ni(II)(L)_2]$ to $[LNi(I)\text{–}L^{\bullet-}]$. Thus, the catalytic cycle begins with the successive two-electron reduction of the Ni(II) centre and the ligand moiety, generating intermediate species **3** through the reductive quenching of the photosensitizer (PS). Next, in the presence of $CO_2$, the reduced species **C** reacts with $CO_2$ to form a $CO_2$ adduct species **4**, as confirmed by *in situ* optical spectroscopic studies under identical photochemical conditions. Species **4** then undergoes a proton-coupled electron transfer (PCET) pathway, leading to the formation of a CO-bound Ni species **6** followed by intermediate species **5**, accompanied by the elimination of $H_2O$. The resulting $Ni^{II}$–CO intermediate can either release CO, regenerate the Ni(II) catalyst, or proceed through a $6e^-/6H^+$ reduction pathway, ultimately forming $CH_4$ as the final product.

Moreover, to further investigate whether the observed photocatalytic activity originates from molecular Ni species or from any *in situ* generated metallic Ni nanoparticles, mercury (Hg) poisoning experiments were performed during photocatalysis. Mercury is known to selectively amalgamate with metallic nanoparticles, thereby suppressing heterogeneous metal-mediated catalytic pathways. Under Hg-treated conditions, the TON values for both CO and $CH_4$ formation exhibited only a marginal decrease (<5%) compared to the standard reaction conditions (Fig. S63). This minimal change indicates that heterogeneous Ni-based species, if formed at all, contribute negligibly to the overall catalytic performance. To further verify the absence of nanoparticle formation, dynamic light scattering (DLS) analyses were conducted during the photocatalytic reaction to monitor the possible generation of colloidal or particulate species. Importantly, no detectable nanoparticles or aggregates were observed throughout the course of catalysis (Fig. S64). Collectively, the Hg poisoning experiments together with the DLS analyses strongly support that the photocatalytic $CO_2$ reduction in this system proceeds predominantly through a homogeneous molecular Ni catalytic pathway, with no evidence for the formation of catalytically active Ni nanoparticles under the applied experimental conditions.

## Mechanistic insight for electrochemical $CO_2$/CO to $CH_4$ conversion in light of DFT calculations

The first electron reduction is metal-centred, converting $Ni^{II}$ to $Ni^I$. DFT analysis of molecular orbitals and spin density

distributions (Fig. S22) indicates spin localization at the Ni centre, consistent with an $S = 1/2$ state. This assignment is corroborated by the EPR spectrum of the reduced complex, which exhibits a rhombic signal ($g = 2.1$, $\Delta g = 0.58$; Fig. S21). The second reduction is ligand-centred, generating the NiI–$L^{\bullet-}$ species. MO and spin density analyses, together with elongation of the N=N bond from 1.269 to 1.333 Å, support occupation of the azo $\pi^*$ orbital. The doubly reduced species (**3**) adopts a triplet ground state ($S = 1$), which is favoured by 0.6 kcal $mol^{-1}$ over the singlet counterpart. This configuration corresponds to independent spin localization on the $Ni^{I}$ centre and the azo-functionalized ligand. The electronic arrangement is further supported by EPR spectroscopy, which shows a signal at $g = 2.076$ with $\Delta g = 0.58$ (Fig. S21). $CO_2$ activation proceeds *via* electron transfer from $Ni^{I}$ to the substrate, affording a $Ni^{II}$–$CO_2^{\bullet-}$ adduct (**4**). Protonation at the pendant $-NH_2$ group produces a hydrogen-bonded [4 + $H^+$] species, where the $CO_2$ radical anion is stabilized by an O···H–N interaction of 1.636 Å. This interaction promotes formation of the Ni–COOH intermediate (**5**) through **TS1** with a computed barrier of 1.83 kcal $mol^{-1}$ (Fig. 7). Intermediate **5** is further stabilized by intramolecular hydrogen bonding between the carboxyl oxygen and the ligand –NH group (1.756 Å), underscoring the critical role of the pendant amine in stabilizing reactive intermediates. The Ni–COOH species undergoes protonation and water elimination to generate the Ni–CO adduct (**6**), completing the two-electron reduction of $CO_2$ to CO. The catalytic cycle then extends beyond CO formation. A second two-electron reduction ($Ni^{II} \rightarrow Ni^{I}$ and $L \rightarrow L^{\bullet-}$) affords intermediate 7 in a triplet spin state ($S = 1$), favoured by 12 kcal $mol^{-1}$ relative to the singlet state. Intermediate **7** engages in PCET *via* **TS2** to form **8**, corresponding to the formal reduction of –CO to –CHO, as supported by elongation of the C–O bond (Fig. 7). A subsequent PCET step converts **8** to **9** *via* **TS3**, which then undergoes further reduction and protonation to afford **10** (Fig. 7). Protonation of **10**, accompanied by water elimination, generates the $Ni^{III}$–$CH_3$ intermediate (**11**). DFT calculations assign a quartet spin state ($S = 3/2$), more stable than the corresponding doublet by 26.8 kcal $mol^{-1}$ (Fig. S65). The Ni oxidation state in **11** is assigned as $Ni^{III}$, supported by *in situ* EPR spectroscopy, which displays diagnostic features distinct from other Ni species (Fig. S21E and F). A final one-electron reduction of **11** yields intermediate **12**, which upon protonation, releases $CH_4$ as the terminal product and regenerates the catalytically active species **1**. Notably, photochemical studies reveal that the same intermediates are accessed under light-driven conditions. Under CO-saturated irradiation at 440 nm in the presence of $CH_3I$, BIH, **Ir-PS-1**, and PhOH; $CH_4$ and $C_2H_6$ were the only gaseous products observed (Fig. S61). Control experiments established that $C_2H_6$ arises from radical coupling between Ni–$CH_3$ and $CH_3I$, whereas omission of $CH_3I$ yielded only $CH_4$. These observations provide direct experimental support for $Ni^{III}$–$CH_3$ (**11**) as a key intermediate under both electrochemical and photochemical regimes. Taken together, the combined DFT and spectroscopic data converge on a unified mechanistic framework for $CO_2$-to-$CH_4$ conversion. In this pathway, the pendant $-NH_2$ group serves as a proton relay, stabilizing reactive intermediates and lowering barriers for PCET events, while cooperative metal–

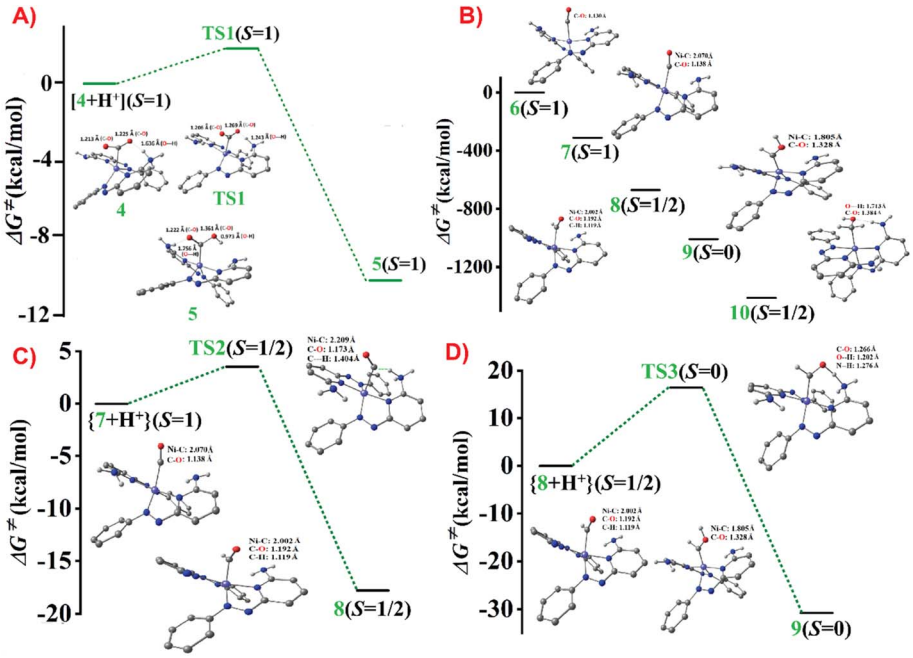


Fig. 7 (A, C and D) The optimized geometry of transition state TS2 highlights a significant secondary coordination sphere coordination sphere effect, characterized by a secondary hydrogen-bonding interaction between the free $-NH_2$ group and the Ni-coordinated $CO_2$ molecule. Relative energies of the various spin states are reported in kcal $mol^{-1}$. All bond distances are given in Å. For clarity, hydrogen atoms are omitted from the structures except for those bonded to the free $-NH_2$ group. (B) Gibbs free energy diagram (kcal $mol^{-1}$) for DFT-optimized structures of six coordinated CO adducts with the $NiL_2$ complex: (**6**) Ni(II)–CO, (**7**) Ni(I)–CO, (**8**) Ni(II)–CHO, (**9**) Ni(II)–CHOH, and (**10**) Ni(I)–$CH_2OH$. Color codes: carbon → gray, hydrogen → white, nitrogen → blue, oxygen → red, and nickel → bluish gray.

ligand redox activity orchestrates the multielectron sequence. Importantly, the same mechanistic principles apply under electrochemical and photochemical conditions, underscoring the generality of **C1** as a dual-active catalyst for selective $CH_4$ evolution.

## Conclusion

This work establishes a redox-active (6-amino-2-(phenylazo) pyridine)–nickel complex (**C1**) as an efficient and sustainable molecular platform for the selective reduction of $CO_2$ to $CH_4$ under both electrochemical and photochemical conditions. Although electrolysis afforded only modest activity, coupling **C1** with visible-light photosensitizers and optimized proton/electron sources resulted in dramatic improvements in efficiency and product selectivity. Notably, Cu(I)-based photosensitizers with tuneable halide bridges were identified as effective, earth-abundant alternatives to Ir-systems, with **Cu-PS-1** delivering turnover numbers (TONs) for $CO_2$-to-CO (4789), $CO_2$-to-$CH_4$ (1130), and CO-to-$CH_4$ (3102) that rival state-of-the-art noble-metal photosensitizers. Comprehensive mechanistic probing, combining DFT with *in situ* EPR, FT-IR, UV-vis, and electrochemical analyses, revealed that catalysis proceeds through a cooperative metal–ligand redox pathway. The Ni centre and azo-functionalized ligand undergo sequential reductions to generate a Ni–$CO_2$ adduct, followed by proton-coupled electron transfer steps leading to $CH_4$. Crucially, the pendant $-NH_2$ functionality facilitates hydrogen bonding to stabilize key COOH and $CH_x$ intermediates and lowers kinetic barriers along the multielectron pathway. Direct detection of a $Ni^{III}$–$CH_3$ species provides experimental support for C–H bond formation as the final step in methane evolution, with identical intermediates observed in both electrochemical and photochemical regimes. Together, these findings define a unified mechanistic framework for **C1**-mediated $CO_2$ reduction and underscore the broader potential of redox-active ligand scaffolds in molecular catalyst design. By demonstrating that earth-abundant transition metals, when paired with properly engineered ligands and photosensitizers, can mediate the full eight-electron conversion of $CO_2$ to $CH_4$, this study establishes design principles for next-generation systems in artificial photosynthesis and carbon valorization. More broadly, this work highlights the promise of integrating low-cost, tuneable molecular architectures with solar energy input to advance sustainable fuel production and scalable carbon recycling technologies.

## Conflicts of interest

C. D. and A. D. have applied for a provisional Indian Patent (Application Number 2024034835) along with IIT Bombay, with a part of the work reported here.

## Abbreviations

| | |
|---|---|
| $CO_2$RR | Carbon-di-oxide reduction reaction |
| FTIR | Fourier transform infrared spectroscopy |
| EPR | Electron paramagnetic resonance |
| TEOA | Triethanolamine |
| TBABF | Tetrabutylammonium tetrafluoroborate |
| CCUS | Carbon capture, utilization, and storage |
| **CzIPN** | 2,4,5,6-Tetra(9*H*-carbazol-9-yl)isophthalonitrile |
| LED | Light-emitting diode |
| PS | Photosensitizer |
| SED | Sacrificial electron donor |
| BIH | 3-Dimethyl-2-phenyl-2,3-dihydro-1*H*-benzo[*d*] imidazole |
| TON | Turn over number |
| PCET | Proton-coupled electron transfer |
| DMA | Dimethylacetamide |
| DFT | Density functional theory |

## Data availability

The data supporting this article have been included as part of the supplementary information (SI). Supplementary information is available. See DOI: https://doi.org/10.1039/d6sc02569b.

## Acknowledgements

The authors would like to acknowledge the Central Instrumental Facility and financial support from the Indian Institute of Technology Bombay (IITB). A. D. acknowledges the funding support from the DST (India)-supported National Centre of Excellence for Carbon Capture, Utilization, and Storage (DST/TMD/CCUS/CoE/202/IITB) and the Ministry of Steel, Government of India (S-20021/19/2024-TECH/19973).

## References

1 D. Kim, K. K. Sakimoto, D. Hong and P. Yang, *Angew. Chem., Int. Ed.*, 2015, **54**, 3259–3266.
2 H. B. Gray, *Nat. Chem.*, 2009, **1**, 7.
3 N. S. Lewis and D. G. Nocera, *Proc. Natl. Acad. Sci. U. S. A.*, 2006, **103**, 15729–15735.
4 S. Nitopi, E. Bertheussen, S. B. Scott, X. Liu, A. K. Engstfeld, S. Horch, B. Seger, I. E. L. Stephens, K. Chan, C. Hahn, J. K. Nørskov, T. F. Jaramillo and I. Chorkendorff, *Chem. Rev.*, 2019, **119**, 7610–7672.
5 P. Majumder and A. Dutta, *iScience*, 2025, **28**(10), 113509.
6 P. Kurz, B. Probst, B. Spingler and R. Alberto, *Eur. J. Inorg. Chem.*, 2006, **2006**, 2966–2974.
7 D. Ghosh, T. Kajiwara, S. Kitagawa and K. Tanaka, *Eur. J. Inorg. Chem.*, 2020, **2020**, 1814–1818.
8 H. Shirley, T. M. Sexton, N. P. Liyanage, C. Z. Palmer, L. E. McNamara, N. I. Hammer, G. S. Tschumper and J. H. Delcamp, *Eur. J. Inorg. Chem.*, 2020, **2020**, 1844–1851.
9 B. M. Rosen, K. W. Quasdorf, D. A. Wilson, N. Zhang, A.-M. Resmerita, N. K. Garg and V. Percec, *Chem. Rev.*, 2011, **111**, 1346–1416.
10 W. Keim, *Angew Chem. Int. Ed. Engl.*, 1990, **29**, 235–244.
11 J.-H. Jeoung and H. Dobbek, *Science*, 2007, **318**, 1461–1464.

12 J. Fesseler, J.-H. Jeoung and H. Dobbek, *Angew. Chem., Int. Ed.*, 2015, **54**, 8560–8564.
13 D. Hong, T. Kawanishi, Y. Tsukakoshi, H. Kotani, T. Ishizuka and T. Kojima, *J. Am. Chem. Soc.*, 2019, **141**, 20309–20317.
14 D. Hong, Y. Tsukakoshi, H. Kotani, T. Ishizuka and T. Kojima, *J. Am. Chem. Soc.*, 2017, **139**, 6538–6541.
15 V. S. Thoi, N. Kornienko, C. G. Margarit, P. Yang and C. J. Chang, *J. Am. Chem. Soc.*, 2013, **135**, 14413–14424.
16 H. Shirley, X. Su, H. Sanjanwala, K. Talukdar, J. W. Jurss and J. H. Delcamp, *J. Am. Chem. Soc.*, 2019, **141**, 6617–6622.
17 E. Kimura, X. Bu, M. Shionoya, S. Wada and S. Maruyama, *Inorg. Chem.*, 1992, **31**, 4542–4546.
18 C. A. Craig, L. O. Spreer, J. W. Otvos and M. Calvin, *J. Phys. Chem.*, 1990, **94**, 7957–7960.
19 J. Schneider, H. Jia, K. Kobiro, D. E. Cabelli, J. T. Muckerman and E. Fujita, *Energy Environ. Sci.*, 2012, **5**, 9502–9510.
20 B. J. Fisher and R. Eisenberg, *J. Am. Chem. Soc.*, 1980, **102**, 7361–7363.
21 X. Su, K. M. McCardle, J. A. Panetier and J. W. Jurss, *Chem. Commun.*, 2018, **54**, 3351–3354.
22 M. F. Kuehnel, K. L. Orchard, K. E. Dalle and E. Reisner, *J. Am. Chem. Soc.*, 2017, **139**, 7217–7223.
23 J. Lin, B. Qin and Z. Fang, *Catal. Lett.*, 2019, **149**, 25–33.
24 H.-H. Huang, J.-H. Zhang, M. Dai, L. Liu, Z. Ye, J. Liu, D.-C. Zhong, J.-W. Wang, C. Zhao and Z. Ke, *Proc. Natl. Acad. Sci. U. S. A.*, 2022, **119**, e2119267119.
25 N.-X. Li, Y.-M. Chen, Q.-Q. Xu and W.-H. Mu, *J. CO2 Util.*, 2023, **68**, 102385.
26 J. Zhang, P. She, Q. Xu, F. Tian, H. Rao, J.-S. Qin, J. Bonin and M. Robert, *ChemSusChem*, 2024, **17**, e202301892.
27 H. Rao, L. C. Schmidt, J. Bonin and M. Robert, *Nature*, 2017, **548**, 74–77.
28 H. Rao, C.-H. Lim, J. Bonin, G. M. Miyake and M. Robert, *J. Am. Chem. Soc.*, 2018, **140**, 17830–17834.
29 A. Rosas-Hernández, P. G. Alsabeh, E. Barsch, H. Junge, R. Ludwig and M. Beller, *Chem. Commun.*, 2016, **52**, 8393–8396.
30 M. S. Lowry, J. I. Goldsmith, J. D. Slinker, R. Rohl, R. A. Pascal, G. G. Malliaras and S. Bernhard, *Chem. Mater.*, 2005, **17**, 5712–5719.
31 T. Bortolato, S. Cuadros, G. Simionato and L. Dell'Amico, *Chem. Commun.*, 2022, **58**, 1263–1283.
32 H. Yuan, Y. Yu, S. Yang, Q. Lei, Z. Yang, B. Lan and Z. Han, *Chem. Commun.*, 2024, **60**, 6292–6295.
33 Y. Wang, L. Chen, T. Liu and D. Chao, *Dalton Trans.*, 2021, **50**, 6273–6280.
34 J. Bonin, M. Robert and M. Routier, *J. Am. Chem. Soc.*, 2014, **136**, 16768–16771.
35 J.-W. Wang, F. Ma, T. Jin, P. He, Z.-M. Luo, S. Kupfer, M. Karnahl, F. Zhao, Z. Xu, T. Jin, T. Lian, Y.-L. Huang, L. Jiang, L.-Z. Fu, G. Ouyang and X.-Y. Yi, *J. Am. Chem. Soc.*, 2023, **145**, 676–688.
36 W. Helweh, P. Kim, Z. J. Mast, B. T. Phelan, N. P. Weingartz, R. Zong, S. Chaudhuri, R. P. Thummel, G. C. Schatz and L. X. Chen, *Inorg. Chem.*, 2024, **63**(32), 14905–14912.
37 M. M. Alowakennu, A. Ghosh and J. K. McCusker, *J. Am. Chem. Soc.*, 2023, **145**, 20786–20791.
38 K. Kiyosawa, N. Shiraishi, T. Shimada, D. Masui, H. Tachibana, S. Takagi, O. Ishitani, D. A. Tryk and H. Inoue, *J. Phys. Chem. C*, 2009, **113**, 11667–11673.
39 N. Nagata, Y. Kuramochi and Y. Kobuke, *J. Am. Chem. Soc.*, 2009, **131**, 10–11.
40 M. C. Rosko, K. A. Wells, C. E. Hauke and F. N. Castellano, *Inorg. Chem.*, 2021, **60**, 8394–8403.
41 H. Takeda, K. Ohashi, A. Sekine and O. Ishitani, *J. Am. Chem. Soc.*, 2016, **138**, 4354–4357.
42 S. Patra, S. Bhunia, S. Ghosh and A. Dey, *ACS Catal.*, 2024, **14**, 7299–7307.
43 S. Guria, D. Dolui, C. Das, S. Ghorai, V. Vishal, D. Maiti, G. K. Lahiri and A. Dutta, *Nat. Commun.*, 2023, **14**, 6859.
44 C. Das, S. Ghosh, A. Guha, P. Majumder, G. K. Lahiri and A. Dutta, *Cryst. Growth Des.*, 2024, **24**(15), 6463–6471.
45 C. Das, S. Ghosh, R. Biswas, G. K. Lahiri and A. Dutta, *Chem. Commun.*, 2024, **60**, 10492–10495.
46 G. Musie, P. J. Farmer, T. Tuntulani, J. H. Reibenspies and M. Y. Darensbourg, *Inorg. Chem.*, 1996, **35**, 2176–2183.
47 P. Prabukanthan, M. Sreedhar, S. Thamaraiselvi, G. Harichandran, P. Seenuvasakumaran, M. M. Hanafiah and C. Fernandez, *J. Mater. Sci.: Mater. Electron.*, 2021, **32**, 6331–6343.
48 L. Gomes, E. Pereira and B. de Castro, *J. Chem. Soc., Dalton Trans.*, 2000, 1373–1379.
49 A. Müller, I. Tscherny, R. Kappl, C. E. Hatchikian, J. Hüttermann and R. Cammack, *J. Biol. Inorg. Chem.*, 2002, **7**, 177–194.
50 A. K and V. Kathirvelu, *J. Phys. Chem. Solids*, 2021, **157**, 110224.
51 N. Sarı, S. Ç. Şahin, H. Öğütcü, Y. Dede, S. Yalcin, A. Altundaş and K. Doğanay, *Spectrochim. Acta, Part A*, 2013, **106**, 60–67.
52 K. Thangavel, P. C. Bruzzese, M. Mendt, A. Folli, K. Knippen, D. Volkmer, D. M. Murphy and A. Pöppl, *Phys. Chem. Chem. Phys.*, 2023, **25**, 15702–15714.
53 G. Sabharwal, K. C. Dwivedi and M. S. Balakrishna, *Appl. Organomet. Chem.*, 2025, **39**, e70322.
54 G. Sabharwal, K. C. Dwivedi, C. Das, T. R. K. Rana, A. Dutta, G. Rajaraman and M. S. Balakrishna, *J. Catal.*, 2024, **440**, 115825.
55 J. D. Froehlich and C. P. Kubiak, *J. Am. Chem. Soc.*, 2015, **137**, 3565–3573.
56 T. Fogeron, T. K. Todorova, J.-P. Porcher, M. Gomez-Mingot, L.-M. Chamoreau, C. Mellot-Draznieks, Y. Li and M. Fontecave, *ACS Catal.*, 2018, **8**, 2030–2038.
57 M. Claros, F. Ungeheuer, F. Franco, V. Martin-Diaconescu, A. Casitas and J. Lloret-Fillol, *Angew. Chem., Int. Ed.*, 2019, **58**, 4869–4874.
58 H. Na and L. M. Mirica, *Nat. Commun.*, 2022, **13**, 1313.
59 I. E. Soshnikov, N. V. Semikolenova, K. P. Bryliakov, A. A. Antonov, W.-H. Sun and E. P. Talsi, *J. Organomet. Chem.*, 2019, **880**, 267–271.
60 M. Valente, C. Freire and B. de Castro, *J. Chem. Soc., Dalton Trans.*, 1998, 1557–1562.

61 A. Awasthi, I. F. Leach, S. Engbers, R. Kumar, R. Eerlapally, S. Gupta, J. E. M. N. Klein and A. Draksharapu, *Angew. Chem., Int. Ed.*, 2022, **61**, e202211345.
62 G. Bender, T. A. Stich, L. Yan, R. D. Britt, S. P. Cramer and S. W. Ragsdale, *Biochemistry*, 2010, **49**, 7516–7523.
63 L. Griego, J. B. Chae and L. Mirica, *ChemRxiv*, 2023, preprint, chemrxiv-2023-fpf1n, DOI: 10.26434/chemrxiv-2023-fpf1n.
64 G. K. Lahiri, L. J. Schussel and A. M. Stolzenberg, *Inorg. Chem.*, 1992, **31**, 4991–5000.
65 I. Bach, R. Goddard, C. Kopiske, K. Seevogel and K.-R. Pörschke, *Organometallics*, 1999, **18**, 10–20.
66 D. Lexa, J. M. Saveant and D. L. Wang, *Organometallics*, 1986, **5**, 1428–1434.
67 A. P. Wilde, K. A. King and R. J. Watts, *J. Phys. Chem.*, 1991, **95**, 629–634.
68 M. G. Colombo, A. Hauser and H. U. Guedel, *Inorg. Chem.*, 1993, **32**, 3088–3092.